Geophys. J. Int. (2006) **164,** 359–369 doi: 10.1111/j.1365-246X.2005.02812.x

Compressional deformation north of the Easter microplate: a manned submersible and seafloor gravity investigation

R. C. Searle,[1] J. Francheteau[2] and R. Armijo[3]

[1] *Department of Earth Sciences, Durham University, South Road, Durham,* DH1 3LE, *UK. E-mail: r.c.searle@durham.ac.uk*
[2] *Institut Universitaire Européen de la Mer, Université de Bretagne Occidentale, Place Nicolas Copernic,* 29280 *Plouzané, France*
[3] *Laboratoire Tectonique, Institut de Physique du Globe,* 4 *place Jussieu,* 75252 *Paris CEDEX* 05, *France*

Accepted 2005 September 20. Received 2005 July 14; in original form 2004 November 12

SUMMARY

We have investigated an E–W compressional ridge in 0.9 Ma lithosphere of the Nazca Plate, just north of the Easter microplate on the East Pacific Rise, using a combination of visual observation and seabed gravity measurements from four manned submersible dives. Three of the dives made a 26-km-long traverse across the ridge during which 14 gravity measurements were made. The observations confirm the presence of active thrust faulting on the 1.1-km-high south face of the ridge. However, the gravity precludes the existence of a simple low-angle thrust, and is only compatible with significant crustal shortening and thickening if the block to the south of the thrust has a lower density than the overriding block. Visual and sonar observations of pervasive fine-scale tectonism in this area lend some support to this idea. Alternatively, there could be oblique thrusting on a high-angle fault with relatively little crustal shortening. In addition, a small degree of crustal shortening may take place in the form of buckling of an elastic or plastic lithosphere, though this cannot explain the strong asymmetry of the ridge, which we believe must imply faulting.

Key words: compression, gravity anomalies, lithospheric deformation, mid-ocean ridges, oceanic lithosphere, plate convergence.

INTRODUCTION

The Easter microplate is a small piece of oceanic lithosphere about 400 km across that is accreting and rapidly rotating between two subparallel branches of the East Pacific Rise (EPR; Herron 1972; Handschumacher *et al.* 1981; Hey *et al.* 1985; Zukin & Francheteau 1990; Naar & Hey 1991; Rusby1992; Rusby & Searle 1995), Fig. 1. Magnetic anomalies, earthquake mechanisms and kinematic modelling show that it is rotating clockwise relative to the Pacific and Nazca plates, which bound it (Anderson *et al.* 1974; Handschumacher *et al.* 1981; Engeln & Stein 1984; Naar & Hey 1991; Schouten *et al.* 1993; Rusby & Searle 1995). The Easter–Nazca pole of relative rotation is near 22.6°S, 112.4°W with a rotation rate of 15° Ma^{-1} (Naar & Hey 1989; Rusby & Searle 1995).

Although most of the neighbouring Pacific and Nazca plates appear to be rigid and undeformed, a small area some 100 km across to the north of the main northern boundary of the microplate appears to be undergoing diffuse compressional deformation as the microplate rotates against the Nazca plate to its north. This deformation is manifested by the production of several major E–W ridges, intraplate seismicity, and anomalies in the recent seafloor spreading history on the East Pacific Rise just to the west of this area (Engeln & Stein 1984; Hey *et al.* 1985; Naar & Hey 1989; Searle *et al.* 1989; Naar & Hey 1991; Rusby & Searle 1993, 1995; Delouis *et al.* 1998). Similar features exist in the corresponding position north of the nearby and similarly evolving Juan Fernandez microplate (Larson *et al.* 1992; Searle *et al.* 1993; Bird *et al.* 1998).

Rusby & Searle (1993) made a detailed study of this area based on long-range sidescan sonar (GLORIA), multibeam echosounding and seismicity data (Fig. 1). At least 10 E–W ridges are located in a broad swathe trending WNW from the northern tip of the microplate's east rift, of which the most prominent are indicated by shading on Fig. 1. All have steep south-facing scarps and gentler N-dipping slopes. Relief is substantial, up to 1.4 km. The positions of the ridges coincide with a broad cluster of earthquakes, several of which have focal mechanism solutions (Dziewonski *et al.* 1981; Engeln & Stein 1984; Delouis *et al.* 1998, Fig. 1). Three of these (1, 5 and 6 in Fig. 1) are strike-slip with their *P* axes along the predicted compressional direction; two (2 and 4) are strike-slip with minor compression. For number 3 the best solution is pure thrust along the predicted compressional direction, though there could be up to 30 per cent strike-slip (Engeln & Stein 1984). Delouis *et al.* (1998) analysed the 1996 May 9 magnitude 7.1 earthquake (number 7) using broad-band data. They showed that the best-fit focal mechanism is a downdip oblique (N60°E) rupture on a low angle (15°) NNE-dipping thrust, with a nucleation depth of 1 ± 1 km below the seafloor.

The tectonic spreading fabric on the Nazca lithosphere around the ridges consists of small-amplitude normal faults and abyssal hills that parallel the present EPR axis. The ridges frequently truncate this

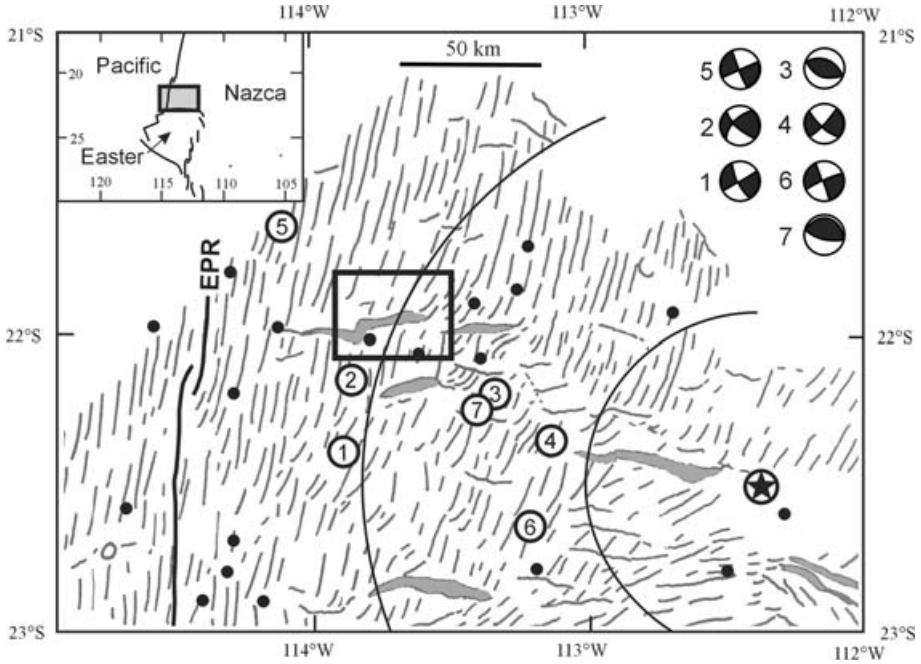

Figure 1. The study area (bold box) and its tectonic setting. Inset shows regional location with plate boundaries. Note that the northern boundary of the Easter microplate lies along the southern boundary of the main figure. Grey lines are tectonic lineaments inferred from GLORIA sidescan images, with the more prominent E–W features shaded. Bold line shows axis of East Pacific Rise. Black dots are earthquake epicentres, and small numbered circles show positions of earthquakes whose focal mechanisms are shown (Dziewonski *et al.* 1981; Engeln & Stein 1984; Delouis *et al.* 1998). Curved lines are small circles about Easter–Nazca pole of rotation shown by circled star (Rusby & Searle 1995). Figure modified from Rusby & Searle (1993).

fabric, whose lineations often exhibit a short dextral swing as the ridges are approached from the north. These swings in the azimuth of the fabric are similar to those that are elsewhere associated with the traces of non-transform offsets (Macdonald *et al.* 1988).

Kinematic modelling using the best-fit Easter–Nazca pole of rotation (−22.7°, −112.3°; Rusby & Searle 1995) predicts compressional relative motion in this region, ranging from very small, N directed motion near the pole, to a maximum of 54 km Ma^{-1} directed along 024° near 22°S, 114°W (Fig. 1). The latter would integrate to a total of about 50 km over the 0.9 Ma age of this seafloor. In fact much of this compressive strain is probably localized along the 'Pito Fracture Zone' (Francheteau *et al.* 1988; Zukin & Francheteau 1990), which demarcates the main northern boundary of the microplate at 23°N. Nevertheless, the ridges to the north have comparable relief to that on the Pito Fracture Zone, suggesting that they may accommodate a significant proportion of the strain, although it is probably distributed between them. Opening rates on the EPR fall from about 152 km Ma^{-1} near 21°S (Perram *et al.* 1990; Naar & Hey 1991; Rusby & Searle 1995) to 130 km Ma^{-1} at 22.6°S (Naar & Hey 1991). This 22 km Ma^{-1} difference has been attributed to extended deformation of the Nazca plate immediately north of 23°S (Searle *et al.* 1989; Perram *et al.* 1990; Naar & Hey 1991; Rusby & Searle 1993). If the horizontal area of the plate is approximately conserved during deformation, the N–S compressional strain should also be about 22 km Ma^{-1}, roughly the average of that predicted by the pole of rotation. The summed strain over the more westerly ridges has been estimated to be of the order of 10 km (Rusby & Searle 1993).

In 1993 November the French manned submersible *Nautile* was deployed on a 21-dive programme around the boundary of the Easter microplate (Francheteau *et al.* 1994; Cogné *et al.* 1995; Hey *et al.* 2002; Searle *et al.* 2003; Naar *et al.* 2004). As part of that programme, four dives were devoted to investigating the compressional deformation in one of the ridges north of the microplate. Major objectives were to determine the nature of the compressional strain using structural observations and the amount of strain using gravity measurements, in order to deduce the amount of crustal thickening. We here report the results of that study.

We find abundant evidence for active faulting on the south-facing scarps, with indications that at least the shallow deformation is by thrust faulting. However, the gravity data show that for a constant density crust the amount of thickening must be quite minor, although the data are compatible with shortening of ∼3.5 km and consequent thickening of ∼1.2 km if the crust south of the ridge has a slightly lower density than that to the north. Alternatively, the ridges might have been formed by oblique, low-rake thrusting along high-dip fault planes. A small amount of compression may be accommodated by plate buckling.

STUDY AREA

Our dives concentrated on the largest of the E–W ridges, which is situated at 21°55′S, 113°40′W (Fig. 2). It is near the northern and western limits of the deformed area, 110 km north of the main microplate boundary and 60 km east of the East Pacific rise axis on seafloor whose 0.9 Ma age is well constrained by magnetic anomalies (Rusby & Searle 1995). This ridge was chosen because of its size, reasonably good bathymetric coverage, and relatively large distance from the Easter–Nazca rotation pole implying the possibility of significant crustal shortening and thickening. The ridge is about 40 km long (Fig. 1), approximately 10 km wide, and has a 10 km N–S jog half way along, which has been interpreted as a sinistral transfer zone (Rusby & Searle 1993). It has a maximum height of 1.4 km. Its southern boundary is a steep escarpment facing south, while the northern flank dips gently to the north; it has a broad, 400-m-deep depression to its south. There is both GLORIA

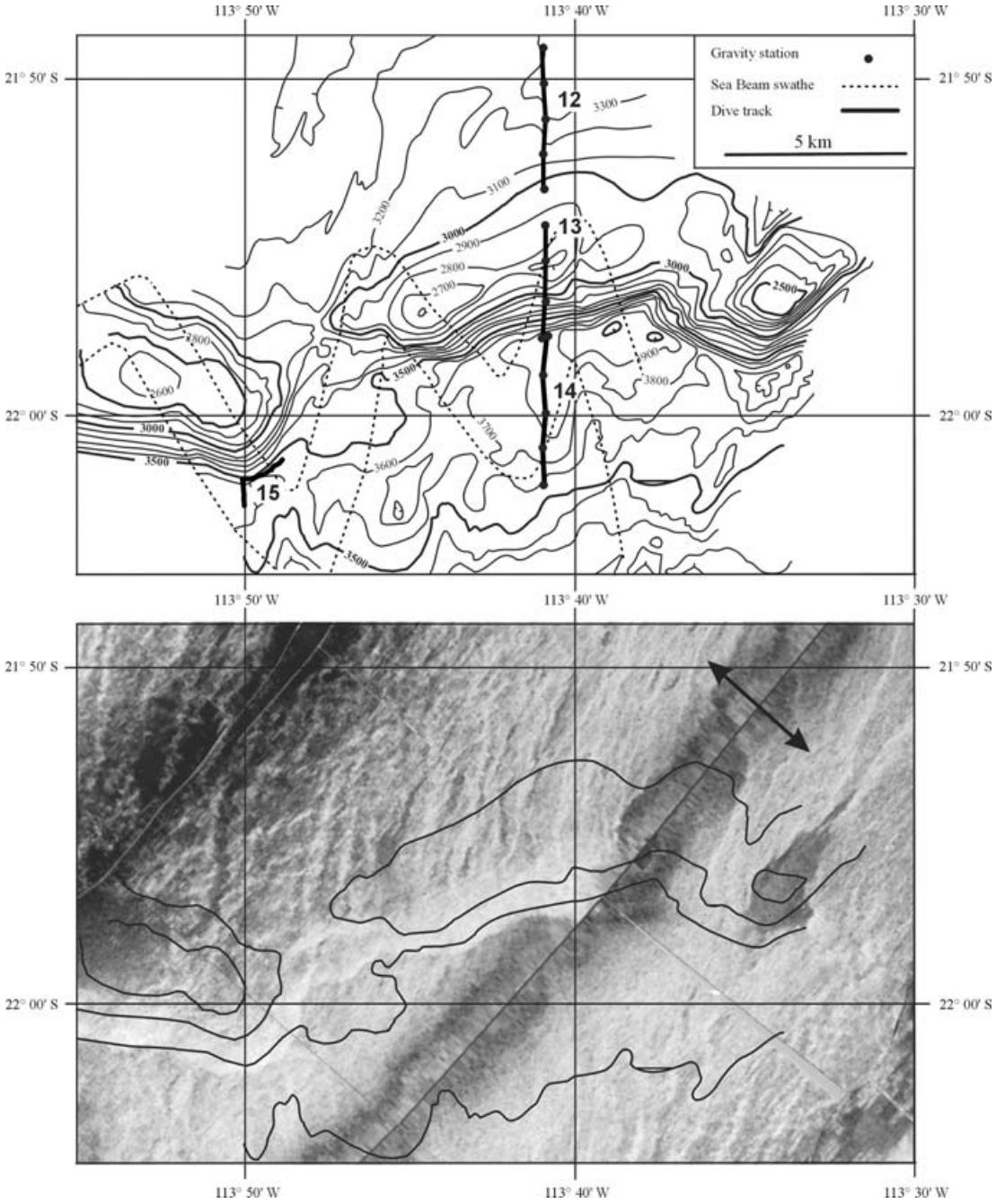

Figure 2. Top: Bathymetric map of the E–W ridge, showing positions of the dive tracks (bold lines), gravity stations (dots) and the Sea Beam swathe (broken lines). Contours (interval 100 metres) derived from Sea Beam and other soundings. Bottom: detail of GLORIA sidescan sonar image (Rusby & Searle 1993) at same scale. Light tones represent high backscatter. The 500 m contours are shown for reference. Oblique line from lower left to upper right is ship-track, and darker zones in top left and lower right corners mark the edges of the sidescan swathe made from this track. Insonification is outwards from the track (arrows); it reverses in the top left corner, which is from a neighbouring swathe. Note strong backscatter from south-facing scarp face, and relatively high backscatter from seafloor south of the ridge compared to that to the north.

sidescan (Searle *et al.* 1989; Rusby & Searle 1993, 1995) and partial Sea Beam bathymetric coverage (Marchig *et al.* 1992; Rusby & Searle 1993). The East Pacific Rise to the west shows no unusual features, although there is a small overlapping spreading centre at 22°08′S (Rusby & Searle 1995). The tectonic spreading fabric around the EW ridges looks normal. Sometimes there is a small dextral swing from 10° in the north to SSW at the ridge crest; it then becomes N–S south of the ridge (Rusby & Searle 1993). An unusual feature of this area is that the GLORIA acoustic backscatter between N–S fault scarps (i.e. what should be normally sedimented seafloor) is considerably higher south of the ridge than to the north (Fig. 2b). This would suggest rougher or less sedimented seafloor, and has been interpreted as evidence of pervasive tectonic disruption in the region (Rusby & Searle 1993).

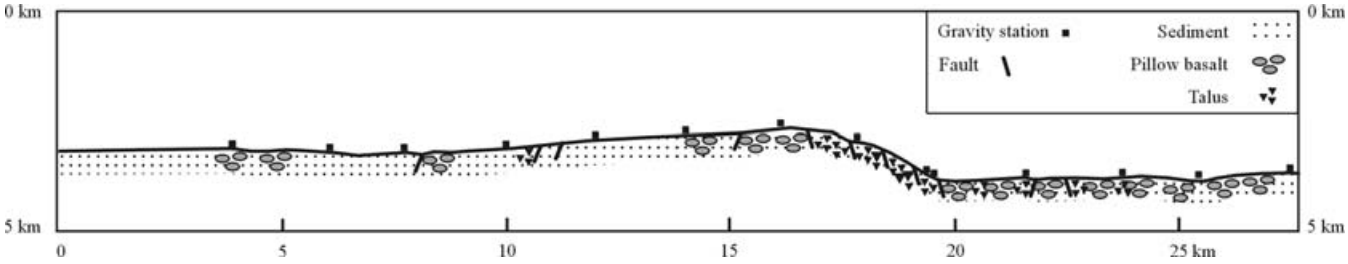

Figure 3. N–S profile produced from the three dives (12–14) across the E–W ridge, showing depth, seafloor lithology, and positions of gravity stations. North to the left. No vertical exaggeration.

THE NAUTILE DIVES

We conducted four dives. All dives except number 12 ran from south to north. Three (dives 12, 13 and 14; observer Searle) together constituted a 26-km-long N–S traverse across the ridge at 113°41′W (Fig. 2). This position was chosen because it is near the centre of one of the linear, E–W parts of the ridge and is covered by a Sea Beam data swathe. At this point the ridge is 1.3 km high. The submersible was navigated by occasional fixes from a short baseline acoustic navigation system and (particularly for dives 12 and 14) by dead reckoning using the submersible's on-board log and gyro between fixes. Gravity measurements were made every 2 km along the traverse, and visual observations were conducted continuously en route between the stations, to build up the seafloor geological section shown in Fig. 3. A fourth dive (dive 15; observer Armijo) investigated the tectonic structures where the escarpment makes contact with the seafloor to the south, near the transfer zone at 113°50′W (Fig. 4). No gravity measurements were made on this dive.

GEOLOGICAL OBSERVATIONS

Observations along the N–S traverse revealed strong contrasts between the seafloor north and south of the escarpment and on the scarp itself (Fig. 3).

North of the escarpment: dive 12 and end of dive 13

The seafloor north of the scarp is mostly undisturbed, as one would expect for 0.9 Ma seafloor. It is characterized by a thin drape of pelagic sediment covering 50 per cent or more of the seafloor, with occasional outcrops of pillow basalt, mostly along old, N–S trending fault scarps that we interpret as having been formed at the East Pacific Rise axis. There are small deposits of fresh talus at the feet of some of these scarps, and occasional fissures characterized by lines of fresh basaltic talus either in shallow linear depressions or on flat, sedimented seafloor. One E–W fault, offset 50 m down to the north, was encountered about 9 km north of the crest of the E–W ridge, but with no fresh talus. Thus, any signs of recent tectonism

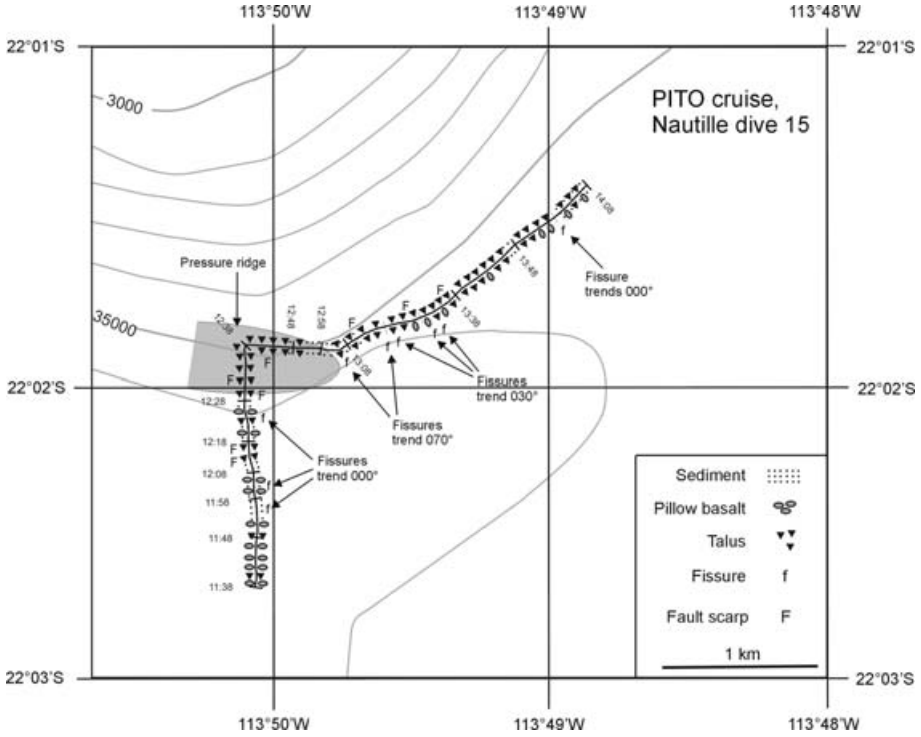

Figure 4. Detailed map of dive 15 along the base of the escarpment, showing depth (contour interval 100 m) and seafloor geology. Local time during dive is written alongside track. The grey area is a schematic representation of the position of a pressure ridge (see text).

north of the ridge are relatively minor. This situation does not change until the very lip of the escarpment, where crevasses appear as the seafloor breaks away under the influence of gravity at the edge of the scarp.

South of the escarpment: dive 14 and first part of dive 15

In contrast, the seafloor south of the escarpment is undergoing active, pervasive, small-scale tectonism. The proportion of sediment-covered seafloor is everywhere less than 50 per cent, with almost no sediment between 1.5 and 3.5 km south of the ridge on dive 14. Between here and the base of the escarpment the sediment cover increases somewhat (though always less than 50 per cent), perhaps as a result of redistribution from the escarpment itself and ponding in the depression at its foot. There are ubiquitous outcrops of pillow basalts, which often display some local fracturing. There are occasional small fault scarps with a variety of trends and some with evidence of recent activity. Occasional narrow, partially open, N–S trending fissures occur, ranging from small, centimetre-wide cracks in pillows, via shallow trenches full of talus, to linear sheets or 'rivers of stone'. These latter are linear deposits hundreds of metres long and up to tens of metres wide, with no discernible vertical relief, and mostly aligned N–S. They are similar to features first seen in the FAMOUS area of the Mid-Atlantic Ridge and described as fissures (Ballard & Moore 1977), although there is no indication of a gap or down-dropped interior. All these fissures follow a trend of approximately 010°, close to that expected for EPR faults, though few such faults were seen. Possibly the fissures are controlled by or mark reactivations of such faults.

More common than these fissures are extensive, flat-lying, fresh, diffuse fields of unsedimented talus. Apparently *in situ* pillows and broken pillows sometimes jut through the talus sheets, giving the impression that the sheets are thin, perhaps only a few metres thick. All of this talus appears to have been formed *in situ*, and is rarely associated with significant scarps or other topographic relief, which is in any case rarely greater than 20 m. The overall impression is of vast areas of pillow basalts, of which 80–100 per cent have been pervasively broken up *in situ*. We interpret the extensive talus as arising from numerous recently active fissures and/or small-scale strike-slip but not dip-slip faulting. This explains the GLORIA data, which show brighter acoustic backscattering south of the escarpment. Overall, the areas of basaltic outcrop and talus are about equal, and together exceed the area of sediment. Except where covered by sediment in the shallow trough at the foot of the scarp, the degree of tectonism and amount of talus and basalt outcrop all increase from south to north as the scarp is approached, although even at the southern end of the traverse, about 8 km south of the scarp, there is more basalt outcrop and less sediment than anywhere north of the scarp.

The foot of the escarpment: end of dive 14 and most of dive 15

Approaching the foot of the escarpment at the end of dive 14, we observed a fine grey dust, inferred to be derived from the break-up of igneous rocks in the escarpment. This began to appear on the surface of the normally cream-to-brown pelagic sediment, starting about 500 m to the south of the scarp. At about 400 m from the scarp we encountered the first of several occurrences of a distinctive, paler, more brown-coloured, finer-grained and blockier talus than the greyer pillow fragments seen farther south. Two samples of this talus taken at station 14-5 at the base of the escarpment proved to be aphyric basalt. A second occurrence of this talus occurred at the end of dive 14 and culminated in a 2-m-high south-facing step—possibly a pressure ridge (see below) with a small sedimented terrace above. This was followed immediately to the north by the start of the main talus ramp of the escarpment.

Dive 15 approached the escarpment from the south on a northerly heading. As on dive 14, the very bottom of the escarpment is marked by a small, south-facing, E–W scarp (about 0.5 m high) at whose crest is a rounded and fissured ridge which we interpret as a pressure ridge (Fig. 4). Again, the main talus ramp begins immediately above this. Above the pressure ridge is a 10-m-high outcrop of older, yellowish, slightly consolidated talus in the form of spurs that taper downwards. These have chutes of active talus between them, which merge into a slope of fresh, homogeneous talus at the base of the outcrop.

Hereafter the submersible turned onto a variable but generally east-north–easterly heading to follow the foot of the escarpment. A similar pressure ridge was encountered intermittently along the foot, just above the contact between flat seafloor and the actively moving talus. It usually had a summit fissure, striking parallel or subparallel to the edge of the escarpment. Both the pressure ridge and the linear break of slope at the foot of the escarpment were often buried under jutting mounds of fresh talus. Small sag ponds and obliquely trending fissures (striking between N–S and 075°) were also encountered. We interpret these observations as indicative of a thrust faulting environment.

The face of the escarpment: dive 13

Dive 13 climbed the entire face of the escarpment where it strikes E–W. As on dive 15, at its foot there is a sharp boundary between a talus wedge and the fairly flat seafloor to the south. The lowermost 100 m of the escarpment consists of pure, well-sorted, unsedimented talus. This comprises both typical pie-slice-shaped pillow fragments and more blocky fragments; samples of both were collected and found to be basalt, not (as initially suspected for the blocks) dolerite from dykes. Above the basal talus pile the scarp face remains extensively covered with fresh talus, but talus sheets parallel to the E–W scarp face are interspersed with talus streams aligned down-slope in the bottoms of gullies that are bounded by outcropping 'buttresses' or spurs like those seen on dive 15. The gullies are spaced a few tens of metres apart and are several metres deep. As on dive 15, the buttresses appear to consist of indurated breccia of pillow fragments in a sediment matrix, but were not sampled. We infer that they are the products of earlier episodes of faulting and mass-wasting. Breccia outcrops, gullies, and talus sheets paralleling the main slope are interspersed up the escarpment.

Between 180 and 750 m above the foot of the scarp, five small, south-dipping faults were seen. Four were E–W and one struck 060°. They were usually recognized by terraces or shallow basins at their crests that are a few metres wide and dip northwards into the main scarp face, and are partially filled with sediment or talus. Some of these faults had exposed faces of breccia just below their crests. A number of fissures were seen near the top of the escarpment, but with no consistent trend. Rather, they appear to control (or be controlled by) the local topography as the top of the slope begins to fail under gravity.

The lowermost 750 m of the scarp has a mean slope of 31°. Above this the slope lessens, the proportion of breccia decreases and the proportion of sediment increases. The talus becomes less well sorted

and the largest blocks get bigger, reaching half-pillow size or larger towards the top. The last talus is 1115 m above the foot of the basal talus ramp and only 30 m below the crest of the escarpment. The average slope over the whole 1.1-km-high escarpment is 28°.

The overall impression of this escarpment is that it is characterized by extensive, active mass wasting. Its top is collapsing under gravity while a talus wedge accumulates at its foot.

GRAVITY MEASUREMENTS

Gravity was measured inside the submersible using a portable 'small case' LaCoste and Romberg geodetic gravity meter. Results are presented in Table 1. Because the 'geodetic' meters have universal scales, there was no need to reset the scale between any of the seabed stations or between ties (for drift) made at the nearest port (Hangaroa, Easter Island). Drift from start to end of the 3-week cruise was 0.2 mGal. At each seafloor station the submersible landed and was made negatively buoyant. It took some 10 min to stabilize, whereupon a reading could be taken. Despite taking great care to minimize movement of personnel, it was hard to keep the submersible completely still, and usually the gravity meter beam retained a residual small oscillation. The estimated reading accuracy was ±0.5 mGal. As a further check, we attempted to repeat one station exactly at the foot of the scarp on separate dives (stations 13-1 and 14-5, Table 1). Because of navigational uncertainties it was impossible to relocate the first station exactly, but post-dive analysis showed they are separated by some 100 m horizontally and 26 m vertically. Their computed free-air anomalies agree to within 3.3 mGal, in a position where the regional free-air gradient is about 38 mGal km^{-1} (Table 1).

Readings were taken on locally flat areas to minimize the effects of poorly known terrain variations near the station. Navigation was by a combination of acoustic navigation at the start and end of each dive, and dead reckoning based on the submersible's log in between. The observed gravity was corrected for latitude and the normal free-air variation, to produce a seabed free-air anomaly (Table 1). The tabled anomalies are relative to the southernmost station on the traverse, arbitrarily taken as zero. Seafloor depth was taken from the submersible's pressure meter.

A 'Free-Water' (Luyendyk 1984) and simple Bouguer anomaly (without terrain correction), computed for crustal densities of 2.4, 2.6 and 2.8 Mg m^{-3}, are shown in Table 1 and Fig. 5. The simple Bouguer anomaly will be affected by terrain effects, which will tend to reduce its value, particularly in the region of the escarpment. Rather than compute terrain corrections explicitly, we implicitly account for the variable terrain in the modelling calculations, as described below.

GRAVITY INTERPRETATION

The simple Bouguer anomaly for all crustal densities shows a minimum at and near the foot of the scarp, which will be due at least in part to terrain effects (Fig. 5). Nevertheless, at the ends of the profile, where these effects should be negligible, the anomalies for all densities are lower at the southern end than at the north. This is the opposite of what would be expected if there were significant crustal thickening under the ridge. Applying Nettleton's (1939) method of estimating densities (i.e. seeking the minimum correlation between Bouguer anomaly and topography), suggests that the most appropriate crustal density is about 2600 kg m^{-3}, although as we show below, detailed modelling suggests a somewhat higher density is more appropriate. However, even with full terrain corrections applied, we find that modelling marine Bouguer anomalies is not particularly intuitive, and instead we prefer to model the free-air anomaly as described below.

Modelling method

The free-air anomaly incorporates corrections for latitude (correcting for the Earth's ellipticity and centrifugal acceleration) and elevation or depth (correcting for distance from the Earth's centre of mass, but not for the local effect of the intervening rock or water). We model the free-air anomaly by computing the complete gravitational effect of the model, including rock and water layers, at the positions of the observation stations on the seabed. The effect of the overlying water layer is thus explicitly included in the modelling. This is equivalent to modelling the seabed Bouguer anomaly as the effect of anomalous masses relative to an assumed constant density rock layer extending down from sea level but, as stated above, is more intuitive, since the whole model is seen, not just the anomalous masses. Modelling used the Talwani 2-D algorithm (Talwani & Heirtzler 1964). This can easily compute the effect of the overlying water layer, but one must ensure that proper account is taken of the quadrant when computing the arctangent for points above the observation level; we

Table 1. Gravity observations.

Station	Depth, m	UTM Y, m	Distance north, km	Latitude, °S	Meter reading, mGal	Free-air anomaly, mGal	Free-water anomaly, mGal	Bouguer anomaly, mGal		
								2400 kg m^{-3}	2600 kg m^{-3}	2800 kg m^{-3}
12-1	3220.0	7,585,030	24.0	21.8170	3082.4	83.9	43.0	15.7	11.8	7.8
12-2	3234.5	7,582,864	21.8	21.8348	3085.0	80.9	41.3	14.9	11.0	7.2
12-3	3254.5	7,581,149	20.1	21.8517	3089.4	78.2	40.2	15.0	11.3	7.6
12-4	3144.0	7,578,833	17.8	21.8728	3074.1	95.6	48.1	16.6	12.0	7.3
12-5	2986.0	7,576,889	15.8	21.8907	3050.8	119.9	58.8	18.1	12.2	6.3
13-4	2856.0	7,574,810	13.8	21.9090	3030.8	139.0	66.6	18.5	11.5	4.5
13-3	2702.0	7,572,720	11.7	21.9282	3006.3	160.8	75.1	18.2	9.9	1.5
13-2	3032.0	7,570,976	9.9	21.9435	3047.6	99.3	42.1	4.1	−1.5	−7.0
13-1	3835.0	7,569,260	8.2	21.9590	3165.6	−31.5	−19.3	−11.3	−10.1	−8.9
14-5	3861.0	7,569,362	8.3	21.9583	3170.3	−34.8	−20.4	−10.8	−9.4	−8.0
14-4	3806.0	7,567,141	6.1	21.9785	3171.5	−17.9	−8.2	−1.8	−0.8	0.1
14-3	3811.0	7,565,018	4.0	21.9975	3173.1	−19.0	−8.9	−2.2	−1.3	−0.3
14-2	3840.0	7,563,250	2.2	22.0302	3177.1	−26.1	−13.5	−5.1	−3.8	−2.6
14-1	3694.0	7,561,043	0.0	22.0333	3158.3	0.0	0.0	0.0	0.0	0.0

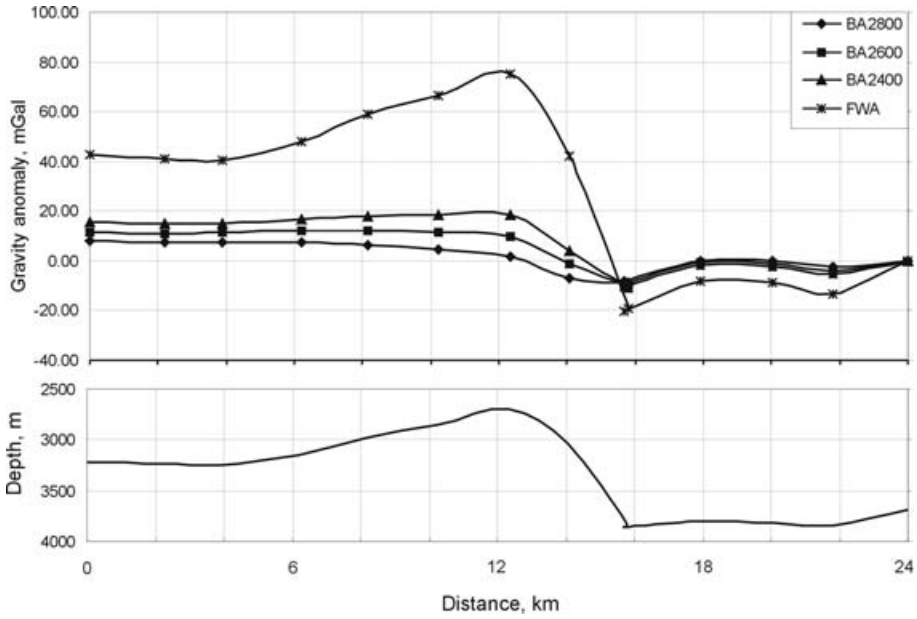

Figure 5. Gravity anomalies (top) above depth profile along the N–S transect. FWA: free-water anomaly; BA2800: Bouguer anomaly for a crustal density of 2800 kg m^{-3}, etc.

found that some common implementations of the algorithm may not do this. By modelling the actual shape of the seafloor profile, a 2-D terrain correction is automatically included. In view of the extreme linearity of the ridge in the region of our profile, any 3-D effects should be small. In order to facilitate comparison between observed and computed anomalies, an arbitrary constant has been added to the observed anomalies in each model so that the average computed anomaly is equal to the average observed anomaly. This is equivalent to adding a small layer of arbitrary constant thickness and density to the base of each model.

Gravity interpretation is notoriously ambiguous, and it is often easy to obtain a good fit by making many minor adjustments to a model, such as the precise position of the Moho or small lateral variations in crustal density. We have avoided this by specifying only a minimum number of constraints in each model. In all the models, sea water and mantle densities were assumed to be 1030 and 3400 kg m^{-3}, respectively. We then explored a range of gravity models in which the only variables were presence or absence of a fault, its dip, the degree of plate convergence and the densities of the crust on either side of the fault. Where crustal convergence is a characteristic of a model, the lower boundary of the crust was determined by conserving the volume of crust as convergence occurs. The main characteristics of typical models are summarized in Table 2, and a selection of these are illustrated in Fig. 6. In addition to the observed and computed gravity anomalies, Fig. 6 shows the calculated vertical stress (i.e. the pressure) at the base of the model, ignoring any dynamic forces such as bending moments. Any departure from a constant stress is a measure of the degree of departure from local isostatic equilibrium.

Modelling results

First, we consider a model in which there is local Airy isostasy everywhere (model 7A, Fig. 6a). This under predicts the observed anomaly by 16 mGal rms (Table 2), clearly showing that the ridge is out of local isostatic equilibrium and must be dynamically supported.

As stated above, it is hard to predict the exact amount of compressive strain that should be associated with this one ridge. The maximum, if all the strain were concentrated here, would be about 50 km. A minimum value is that required to produce the observed 1.1 km of vertical offset. In the latter case, assuming a 20° thrust with motion perpendicular to the ridge yields a horizontal shortening of 3.5 km for local crustal thickening of up to 1.1 km. Such a crustal section should yield a seafloor gravity anomaly of up to 21 mGal compared to a uniform crust.

Fig. 6(c) shows such a model (model 3A) with a constant crustal density of 2800 kg m^{-3}, 3.5 km of shortening, and a thrust fault dipping at 20° to the north. There are rms and maximum misfits of 4.9 mGal and 7.9 mGal, respectively, between observed and modelled anomalies, for what was thought to be a realistic, even minimal, model of crustal shortening. Using a lower crustal density of 2600 kg m^{-3} (model 3E, Table 2) yields a much worse fit (misfit 12.5 mGal rms, 20.8 mGal maximum).

Surprisingly, the best fit between observed and modelled anomalies is for a uniform crust of constant thickness and density (model 2A, Fig. 6b). This gives rms and maximum misfits of 2.0 and 5.0 mGal, respectively, which is considered to be acceptable in view of the estimated observational errors. The average crustal density of 2800 kg m^{-3} in this model is quite high for oceanic crust, but as with the thrust model, lower values give a poorer fit. For example, a value of 2600 kg m^{-3} gives rms and maximum misfits of 4.2 and 8.9 mGal (model 1A, Table 2), although this is still marginally better than model 3A with crustal thickening. Using a multilayer crust makes little difference to the model fit. Other configurations with a crustal density of 2600 kg m^{-3} also give poor fits (models 3E, 5B, Table 2).

That the best-fit model would have a constant crustal thickness was completely unexpected, and suggests that the observed ridge topography may be entirely dynamically supported with little or no crustal thickening. However, a possible resolution is suggested by the observation of pervasive tectonism on the seafloor south of the ridge. If this tectonism has lowered the crustal density of the overridden block by extensive fissuring, the gravity can be successfully

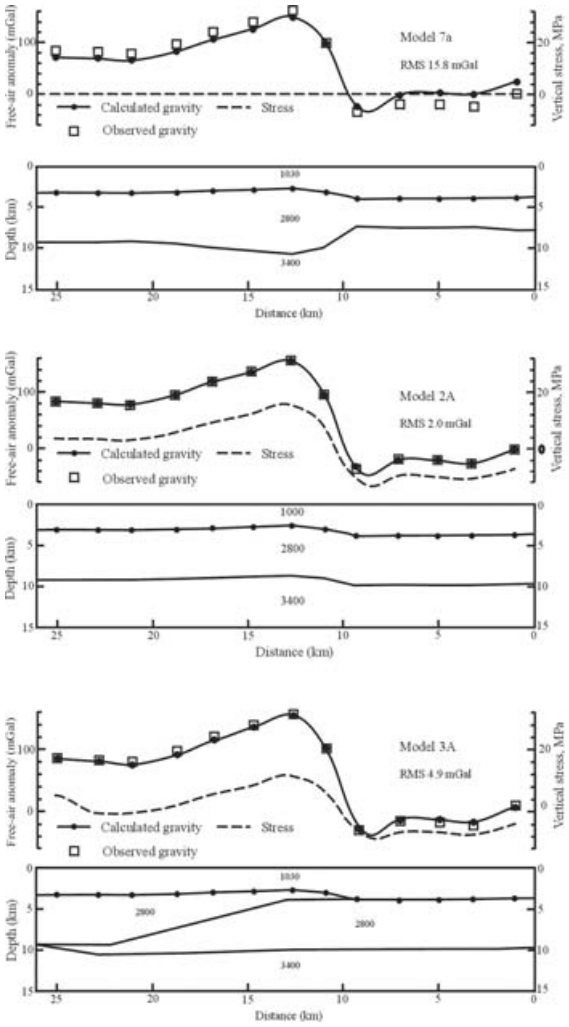

Figure 6. Examples of gravity models. North is to the left. Each panel shows the observed free air anomaly (squares, size approximately equal to observational uncertainty) together with modelled gravity (dots, joined by smooth line) and vertical stress, that is, pressure at the base of the model relative to the mean stress (dashed line), above the 2-D model with density in kg m^{-3}. 'rms' is root-mean-square residual anomaly. Dots on model show positions of seafloor gravity measurements. Vertical exaggeration of models is approximately 0.44. Preferred model (4B) is emphasized. (a) Model 7A, crustal density 2800 kg m^{-3} in local Airy isostatic equilibrium relative to a 6-km-thick crust at the left hand (northern) edge of the model. (b) Model 2A, with constant thickness (6 km) crust of uniform density 2800 kg m^{-3}. Using a crustal density of 2600 kg m^{-3} (model 1A, see Table 2) more than doubles the rms misfit to 4.2 mGal. (c) Model 3A, representing 3.5 km of crustal shortening along a 20° thrust fault and consequent 1.1 km crustal thickening, with 2800 kg m^{-3} crust. Using a crustal density of 2600 kg m^{-3} (model 3E, Table 2) increases the rms misfit to 12.5 mGal. (d) Preferred model (4B), showing the same shortening and crustal thickening as model 3A, but with crustal density of 2800 kg m^{-3} north of the ridge and slightly lower density of 2750 kg m^{-3} to the south. A similar model with the intracrustal density boundary along the 20° fault plane (model 4E, Table 2) yields a slightly greater rms misfit of 3.7 mGal. (e) Model 5, showing the same convergence as models 3A and 4B but on a 45° fault. See text for further discussion.

modelled with the same crustal thickening as used in Fig. 6(c). If we retain a density of 2800 kg m^{-3} for the northern (overriding) block and reduce the density of the southern block by 50 kg m^{-3} to 2750 kg m^{-3}, with the boundary between the two densities along a

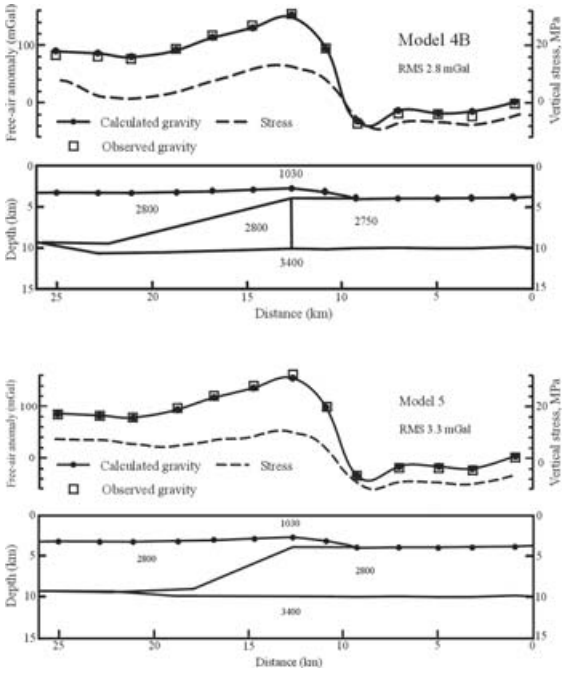

Figure 6. (*Continued.*)

20° N-dipping fault, we achieve a somewhat improved fit with rms and maximum misfits of 3.7 and 7.6 mGal (model 4E, Table 2). Although we might expect this lower density to characterize the whole of the footwall block, a slightly better fit (rms and maximum residuals of 2.8 and 6.1 mGal) is obtained if the low-density crust is confined to the area south of the ridge crest (model 4B, Fig. 6d). This degree of misfit is only slightly worse than that for the constant crustal thickness model 2A.

We may expect lowered densities in the brecciated crust under the escarpment itself. However, modelling this does not improve the fit. For instance, reducing the density of the overriding wedge south of the ridge crest and shallower than the ridge foot to 2600 kg m^{-3} in model 4B increases the rms misfit from 2.8 to 4.0 mGal; lower densities make the fit even worse.

So far we have considered low-angle thrusting, but in theory a thrust could dip up to 45°. Models 5, 5A, 5B and 6 consider this case. The best fit (3.3 mGal rms) is for model 5 with a constant 2800 kg m^{-3} crust (Fig. 6e), almost as good as model 4B.

It is possible that a component of compressional motion can be accommodated on a higher angle fault if the net motion is oblique to the fault plane, so that the rake (the dip of the component of relative motion along the fault plane) does not exceed 45°; in other words, transpressional faulting. The predicted relative motion direction from the Nazca–Easter pole where our traverse crosses the ridge is 028° (Fig. 1), and thrusting at 45° dip along 028° then resolves into a dip of 48.6° along our traverse, so the difference is not very great.

In conclusion, model 4B is our best fit and, therefore, preferred model, and as such is highlighted on Fig. 6. However, a model with a higher angle fault such as model 5 cannot be completely ruled out.

DISCUSSION

We now compare our results with observed focal mechanisms and with other regions of oceanic intraplate compression, and also

Table 2. Summary of gravity models.

Model	Crustal density, kg m^{-3}	Crustal density boundary	Crustal thickness, km	Observed peak-to-trough, mGal	Calculated peak-to-trough, mGal	Peak-to-trough misfit, mGal	Maximum misfit, mGal	RMS misfit, mGal
1A	2600	None	6.0	195.6	180.6	15.0	8.9	4.2
2A	2800	None	6.0	195.6	189.6	6.0	5.0	2.0
3A	2800	20° fault	6.0 to 7.2	195.6	186.8	8.8	7.9	4.9
3E	2600	20° fault	6.0 to 7.2	195.6	176.5	19.1	20.8	12.5
4B	2750, 2800	Vertical	6.0 to 7.2	195.6	190.3	5.3	6.1	2.8
4E	2750, 2800	20° fault	6.0 to 7.2	195.6	188.3	7.3	7.6	3.7
5	2800	45° fault	6.0 to 7.2	195.6	188.1	7.5	6.5	3.3
5A	2750, 2800	45° fault	6.0 to 7.2	195.6	190.4	5.2	7.4	4.0
5B	2600	45° fault	6.0 to 7.2	195.6	178.4	17.2	12.1	6.2
6	2800	45° fault	6.0 to 7.2	195.6	188.4	7.2	6.6	3.0
7A	2800	None	3.5 to 8.1	195.6	177.1	18.5	25.5	15.8

consider the mechanism of the deformation, whether by plate buckling or by reverse (thrust) faulting.

Focal mechanisms

The best-constrained focal mechanism near our study area is that of the 1996 May 9 event, giving slightly oblique rupture on a thrust dipping 15° to the NNE (Delouis *et al.* 1998). This was obtained by careful modelling of broad-band data. In contrast, Delouis *et al.* (1998) report that the routine Harvard Centroid Moment Tensor solution gives a NNE dip of 60°, but point out that parameters determined by this method are less well constrained for shallow earthquakes such as this. Although we did not attempt to model Delouis *et al.*'s result explicitly, our preferred model, with a 20° N-dipping thrust, is in reasonable agreement with their mechanism.

Other areas of oceanic intraplate compression

We consider three areas of significant intraplate deformation that may be relevant to our study area: the Central Indian Ocean, the Gulf of Cadiz area of the eastern Atlantic, and the southern end of the Juan de Fuca plate. All three display rather greater deformation than exhibited north of Easter Microplate, but similar mechanisms may occur at Easter, albeit at a smaller scale.

The Central Indian Ocean is a region of broad lithospheric buckling at wavelengths ∼200 km with topographic amplitudes ∼3 km and gravity anomalies 30–80 mGal (Weissel *et al.* 1980). There is superimposed a smaller-scale deformation (wavelength ∼7 km) comprising reverse faulting in the igneous crust and sediments and associated folding in the sediment section (Bull *et al.* 1992; Bull & Scrutton 1992; van Orman *et al.* 1995). The affected plate has a range of ages up to many tens of Ma. The reverse faults dip 30–40° in the igneous crust and steepen upwards in the sediments to near vertical (Bull & Scrutton 1992), but many of these may be reactivated normal faults formed near the ridge axis (Bull & Scrutton 1992; van Orman *et al.* 1995). Lithospheric shortening of between 11 and 37 km has been estimated at rates of 1–7 mm a^{-1} over ∼1000 km to give total strains of 1–4 per cent since the Late Miocene or a strain rate of about 10^{-16} s^{-1} (Bull & Scrutton 1992; Chamot-Rooke *et al.* 1993; van Orman *et al.* 1995). Earthquake focal mechanisms are mostly strike-slip with a few thrust solutions. The region is generally considered to be a broad, diffuse plate boundary (Gordon *et al.* 1990).

The Gulf of Cadiz is a region of Mesozoic lithosphere and has also suffered relatively recent compressional deformation (Purdy 1975; Hayward *et al.* 1999). Here too deformation is distributed over a wide region (about 300 km), and consists of broad-scale lithospheric warping with a wavelength up to 60 km, and superimposed sediment folding and reverse faulting, some of which is relatively high angle, very similar to the Central Indian Ocean (Tortella *et al.* 1997; Hayward *et al.* 1999). A number of compressional ridges, of which the largest is Gorringe Bank, occur here. The region has been interpreted in terms of faulting (Morel & Meghraoui 1996; Tortella *et al.* 1997), folding (Sartori *et al.* 1994; Girardeau *et al.* 1998) or both (Bergeron & Bonnin 1991; Hayward *et al.* 1999). Gorringe Bank itself is a linear ridge, some 200 km long by 80 km wide and 5 km high, and exposes gabbros and peridotites (Girardeau *et al.* 1998). It is associated with a free-air anomaly of some 350 mGal and has an unsupported mass anomaly of some 10^7 kg m^{-2} (Sartori *et al.* 1994; Hayward *et al.* 1999; Galindo-Zaldívar *et al.* 2003). These authors interpreted the Bank as a large lithospheric block thrust northwestwards over a down-warped plate, with total convergence ∼20 km developed over 5 Ma: a strain rate of about 4×10^{-16} s^{-1}. It may be an incipient subduction zone.

The southern end of the Juan de Fuca plate (sometimes referred to as the Gorda plate), is under shear and compression following a recent clockwise change to the Juan de Fuca—Pacific relative motion (Silver 1971; Wilson 1989). The age of the deformed plate ranges from near zero up to about 6 Ma. However, rather than the plate deforming by buckling or thrusting, the shortening appears to be taken up by rotation and strike-slip motion along pre-existing ridge-parallel normal faults (Masson *et al.* 1989; Wilson 1989) and possibly also an antithetic strike-slip fault set (Wilson 1989). The strain rate has been estimated at about 10^{-14} s^{-1} (Wilson 1989).

These studies indicate that in some respects the deforming region north of the Easter microplate has similarities with both the Central Indian Ocean and the Gulf of Cadiz. The scale at Easter is considerably smaller, since the deforming zone there is only about 100 km across and the individual compressional ridges are three to ten times smaller in all dimensions than Gorringe Bank. The lithosphere at Easter, with a maximum age of about 5 Ma in the east, is much younger and presumably weaker, and the sediment cover is negligible. Moreover, the ridge and escarpment that we studied exposes only upper crustal lithologies (basalts), not gabbro or serpentinite. Nevertheless, as we shall argue below, this area also seems to be deforming under compression by a combination of lithospheric flexure and thrust faulting. However, the southern end of the Juan de Fuca plate is deforming by a very different mechanism, even though its setting, as young lithosphere near an actively spreading ridge, is superficially similar to that north of Easter microplate. The difference

may be that, unlike Juan de Fuca, there is no strong shear couple north of Easter, and the required shortening cannot be taken up by shear along the existing NNE–SSW tectonic fabric.

Buckling or thrusting?

Our gravity results are most consistent with a model in which no variation in crustal thickness occurs, implying pure folding or buckling. If we assume that the whole of the deformation in our studied ridge results from simple lithospheric buckling, then the amount of shortening involved is only about 200 m (i.e. the distance along the seafloor over the ridge compared with the horizontal distance across it), though this occurs over a horizontal distance of about 12 km giving a strain of 1.7 per cent and a strain rate of about 6×10^{-16} s^{-1}. This strain rate is comparable to estimates from the Central Indian Ocean and Gulf of Cadiz, though all are about two orders of magnitude slower than the 10^{-14} s^{-1} that Wilson (1989) considered appropriate for the southern Juan de Fuca plate.

Several authors have modelled the deformation in the Central Indian Ocean. A purely elastic plate would reach its fracture strength before buckling occurred (Weissel *et al.* 1980), but a faulted elastic plate (Wallace & Melosh 1994) or a plastic plate with overlying brittle layer (McAdoo & Sandwell 1985; Bull *et al.* 1992; Martinod & Davy 1992) would buckle first. Numerical modelling suggests that the buckling wavelength is about four times the thickness of the brittle layer (Martinod & Davy 1992), though analogue modelling gives a wavelength that is seven times the brittle thickness (Bull *et al.* 1992).

The wavelength of deformation at Easter is approximately 25 km, so using the relationships of Martinod & Davy (1992) or Bull *et al.* (1992) gives a brittle layer thickness of 3.6–6.2 km. This would imply that about half to all of the crust has a plastic rheology. This might be true for crust near the spreading centre and actively deforming there, or for the crust south of the ridge where we have observed active deformation. However, the crust north of the ridge, which nevertheless is flexed up toward it, shows little sign of recent faulting. Alternatively, flexure in this very young (<1 Ma) lithosphere may be at least partly elastic. Neves *et al.* (2003) used the lithospheric age–thickness relationship of Wang & Cochran (1993) to show that the elastic thickness in the deforming region north of Easter microplate should be about 1–2 km; such lithosphere would have a buckling wavelength of 25–34 km (McAdoo & Sandwell 1985 eq. 5), in accordance with our observations.

Despite these considerations, not all of the deformation in our study area can be due to buckling alone, for two reasons. First, the structural observations, particularly the existence of pressure ridges and sag ponds at the base of the escarpment, directly suggest thrusting. Secondly, in the absence of strong lithospheric heterogeneities, buckling should be roughly symmetric (as it is in the Central Indian Ocean). It is difficult to see how simple folding could give rise to a strongly asymmetric structure with a 31° slope on one side and gentle gradients (∼3°) on the other, without invoking recumbent (overturned) folding, which itself would produce significant crustal thickening.

Interestingly, a similar zone of apparent deformation north of the Juan Fernandez microplate shows ridges that appear to be more symmetric (Larson *et al.* 1992; Bird *et al.* 1998). It is possible that there has been relatively less thrusting and more buckling there, but we note that, unlike the continuous compression at Easter microplate (Rusby & Searle 1995), the northern boundary region of Juan Fernandez Microplate has suffered episodes of transtension as well as transpression (Bird *et al.* 1998).

One might speculate that deformation in younger lithosphere with a thinner brittle layer would be by buckling, with more thrusting occurring in older, thicker lithosphere. This would suggest that those ridges nearest the EPR would be predominantly flexural and, therefore, symmetric, but this is not born out by the sidescan data and the fact that the very asymmetric ridge in our study area is the one closest to the EPR.

It appears then that the ridges north of Easter microplate have formed by a combination of buckling (yielding just a few hundred metres of crustal shortening) and thrusting, possibly on relatively high-angle faults, accommodating up to a few kilometres of shortening.

Finally, we note that the ridge that we studied is not in isostatic equilibrium. A model with local Airy isostasy is a very poor fit to the data. The best-fitting models have unsupported mass loads of around 1.6×10^6 to 2.3×10^6 kg m^{-2} (equivalent to vertical differential stresses of 16–23 MPa), yielding vertical differential stresses ∼20 MPa, which are readily supportable by the lithosphere. By contrast, major features such as Gorringe Bank have mass anomalies almost an order of magnitude greater (Hayward *et al.* 1999).

CONCLUSIONS

(i) Visual observations confirm that active faulting is associated with the E–W ridge, and that pervasive tectonism characterizes the seafloor to its south, but not to the north.

(ii) Seafloor gravity observations indicate that the ridge is dynamically supported, but are not consistent with significant crustal shortening or thickening unless it is assumed that the tectonized crust to the south is of lower density than the unaffected crust to the north.

(iii) We think it most likely that both buckling of the lithosphere and faulting contribute to the deformation north of the Easter microplate.

ACKNOWLEDGMENTS

This work was partly supported by Natural Environment Research Council grant GR9/840 to RCS. We thank Roger Hipkin of Edinburgh University for the loan of a small-case gravity meter. We are grateful to Milène Cormier and an anonymous reviewer for very helpful comments. We thank the IFREMER personnel, Captain and crew of the R/V Nadir and the Nautile team for a successful expedition and the scientific team for their collaboration. The PITO expedition was funded by IFREMER and CNRS.

REFERENCES

Anderson, R.N., Forsyth, D.W., Molnar, P. & Mammerickx, J., 1974. Fault plane solutions on the Nazca plate boundaries and the Easter plate, *Earth planet. Sci. Lett.,* **24,** 188–202.

Ballard, R.D. & Moore, J.E., 1997. *Photographic Atlas of the Mid-Atlantic Ridge Rift Valley*, 114 pp., Springer-Verlag, Heidelberg.

Bergeron, A. & Bonnin, J., 1991. The deep structure of Gorringe bank (NE Atlantic) and its surrounding area, *Geophys. J. Int.,* **105,** 491–502.

Bird, R.T., Naar, D.F., Larson, R.L., Searle, R.C. & Scotese, C.R., 1998. Plate tectonic reconstructions of the Juan Fernandez microplate: transformation from internal shear to rigid rotation, *J. geophys. Res.,* **103,** 7049–7067.

Bull, J.M. & Scrutton, R.A., 1992. Seismic reflection images of intraplate deformation, central Indian Ocean, and their tectonic significance, *J. geol. Soc. Lond.,* **149,** 955–966.

Bull, J.M., Martinod, J. & Davy, P., 1992. Buckling of the oceanic lithosphere from geophysical data and experiments, *Tectonics,* **11,** 537–548.

Chamot-Rooke, N., Jestin, F., de Voogd, B. & the PHEDRE team, 1993. Intraplate shortening in the central Indian Ocean from a 2100 km long north-south deep seismic reflection profile, *Geology,* **21,** 1043–1046.

Cogné, J.P., *et al*., 1995. Large rotation of the Easter microplate as evidenced by oriented paleomagnetic samples from the ocean floor, *Earth planet. Sci. Lett.,* **136,** 213–222.

Delouis, B., Nicolas, A., Ildefonse, B. & Philip, H., 1998. Earthquake focal mechanism and oceanic thrust in Easter microplate analogy with Oman ophiolite, *Geophys. Res. Lett.,* **25,** 1443–1446.

Dziewonski, A.M., Chou, T.-A. & Woodhouse, J.H., 1981. Determination of earthquake source parameters from waveform data for studies of global and regional seismicity, *J. geophys. Res.,* **86,** 2825–2852.

Engeln, J.F. & Stein, S., 1984. Tectonics of the Easter plate, *Earth planet. Sci. Lett.,* **68,** 259–270.

Francheteau, J. *et al*., 1988. Pito and Orongo fracture zones: the northern and southern boundaries of the Easter microplate (southeast Pacific), *Earth planet. Sci. Lett.,* **89,** 363–374.

Francheteau, J. *et al*., 1994. Black smoker discovered, Pito Seamount near Easter microplate propagator tip, *EOS, Trans. Am. geophys. Un.,* **75,** 322.

Galindo-Zaldívar, J., Maldonado, A. & Schreider, A.A., 2003. Gorringe Ridge gravity and magnetic anomalies are compatible with thrusting at a crustal scale, *Geophys. J. Int.,* **153,** 586–594.

Girardeau, J. *et al*., 1998. Extensional tectonics in the Gorringe Bank rocks, eastern Atlantic Ocean: evidence of an oceanic ultra-low mantellic accreting centre, *TerraNova,* **10,** 330–336.

Gordon, R.G., DeMets, C. & Argus, D.F., 1990. Kinematic constraints on distributed deformation in the equatorial Indian Ocean from present motion between the Australian and Indian plates, *Tectonics,* **9**, 409–422.

Handschumacher, D.W., Pilger, R.H., Foreman, J.A. & Campbell, J.F., 1981. Structure and evolution of the Easter plate, *Memoir of the Geological Society of America,* **154,** 63–76.

Hayward, N., Watts, A.B., Westbrook, G.K. & Collier, J.S., 1999. A seismic reflection and GLORIA study of compressional deformation in the Gorringe Bank region, eastern North Atlantic, *Geophys. J. Int.,* **138,** 831–850.

Herron, E.M., 1972. Two small crustal plates in the South Pacific near Easter Island, *Nature Physical Science,* **240,** 35–37.

Hey, R.N., Naar, D.F., Kleinrock, M.C., Phipps Morgan, W.J., Morales, E. & Schilling, J.-G., 1985. Microplate tectonics along a superfast seafloor spreading system near Easter Island, *Nature,* **317,** 320–325.

Hey, R.N. *et al*., 2002. Preliminary attempt to characterize the rotation of seafloor in the Pito Deep area of the Easter microplate using a submersible magnetometer, *Marine Geophysical Researches,* **23,** 1–12.

Larson, R.L. *et al*., 1992. Roller-bearing tectonic evolution of the Juan Fernandez microplate, *Nature,* **356,** 571–576.

Luyendyk, B.P., 1984. On-bottom gravity profile across the East Pacific Rise crest at 21°n, *Geophysics,* **49,** 2166–2177.

Macdonald, K.C. *et al*., 1988. A new view of the mid-ocean ridge from the behaviour of ridge-axis discontinuities, *Nature,* **335,** 217–225.

Marching, V. *et al*., 1992. *Abschussbericht Geometsp 5 (So62)*, 565pp., Bundesanstalt für Gewissenschaften und Rohstoffe, Hanover.

Martinod, J. & Davy, P., 1992. Periodic instabilities during compression or extension of the lithosphere: 1, deformation modes from an analytical perturbation method, *J. geophys. Res.,* **97,** 1999–2014.

Masson, D.G., Cacchione, D.A. & Drake, D., 1989. Tectonic evolution of Gorda Ridge inferred from sidescan sonar images, *Marine Geophysical Researches,* **10,** 191–204.

McAdoo, D.C. & Sandwell, D.T., 1985. Folding of the oceanic lithosphere, *J. geophys. Res.,* **90,** 8563–8569.

Morel, J. & Meghraoui, M., 1996. Gorringe-Alboran-Tell tectonic zone – a transpression system along the Africa-Eurasia plate boundary, *Geology,* **24,** 755–758.

Naar, D.F. & Hey, R.N., 1989. Recent Pacific-Easter-Nazca plate motions, in *Evolution of Mid Ocean ridges*, pp. 9–30, ed. Sinton, J.M., American Geophysical Union, Washington, DC.

Naar, D.F. & Hey, R.N., 1991. Tectonic evolution of the Easter microplate, *J. geophys. Res.,* **96,** 7961–7973.

Naar, D.F. *et al*., 2004. Hydrothermal venting at Pito Seamount near Easter Island, in *Mid-ocean ridges: hydrothermal interactions between the lithosphere and oceans: Geophysical Monongraph 148*, eds German, C., Lin, J. & Parson, L., American Geophysical Union, Washington, DC.

Nettleton, L.L., 1939. Determination of density for reduction of gravimeter observations, *Geophysics,* **4,** 176–183.

Neves, M.C., Searle, R.C. & Bott, M.H.P., 2003. Easter microplate dynamics, *J. geophys. Res.,* **108,** ETG14, doi:10.1029/2001JB000908, citation no. 002213.

Perram, L.J., Macdonald, K.C. & Miller, S.P., 1990. Deep-tow magnetics near 20°s on the East Pacific Rise: a study of short wavelength anomalies at a very fast spreading center, *Marine Geophysical Researches,* **12,** 235–245.

Purdy, G.M., 1975. The eastern end of the Azores-Gibraltar plate boundary, *Geophys. J. R. astr. Soc.,* **43,** 973–1000.

Rusby, R.I., 1992. Tectonic Pattern and history of the Easter Microplate, based on GLORIA and other geophysical data, *PhD thesis*, University of Durham.

Rusby, R.I. & Searle, R.C., 1993. Intraplate thrusting near the Easter microplate, *Geology,* **21,** 311–314.

Rusby, R.I. & Searle, R.C., 1995. A history of the Easter microplate, 5.25 ma to present, *J. geophys. Res.,* **100,** 12 617–12 640.

Sartori, R., Torelli, L., Zitellini, N., Peis, D. & Lodolo, E., 1994. Eastern segment of the Azores-Gibraltar plate boundary (central-eastern Atlantic): an oceanic plate boundary with diffuse compressional deformation, *Geology,* **22,** 555–558.

Schouten, H., Klitgord, K.D. & Gallo, D.G., 1993. Edge-driven microplate kinematics, *J. geophys. Res.,* **98,** 6689–6701.

Searle, R.C., Rusby, R.I., Engeln, J., Zukin, J., Hunter, P.M., LeBas, T.P., Hoffman, H.-J. & Livermore, R., 1989. Comprehensive sonar imaging of the Easter microplate, *Nature,* **341,** 701–705.

Searle, R.C., Bird, R.T., Rusby, R.I. & Naar, D.F., 1993. The development of two oceanic microplates: Easter and Juan Fernandez microplates, east pacific rise, *J. geol. Soc. Lond.,* **150,** 965–976.

Searle, R.C., Armijo, R. & Francheteau, J., 2003. Manned submersible and seafloor gravity investigation of a compressional ridge in young oceanic lithosphere near the Easter microplate, *Geophysical Research Abstracts,* **5,** 06724.

Silver, 1971. Tectonics of the Mendocino triple junction, *Geological Society of America Bulletin,* **82,** 2965–2978.

Talwani, M. & Heirtzler, J.R., 1964. Computation of magnetic anomalies caused by two-dimensional structures of arbitrary shape, *Computers in the Mineral Industries1, Stanford University Publications in the Geological Sciences,* **9,** 464–480.

Tortella, D., Torne, M. & Pérez-Eastaún, 1997. Geodynamic evolution of the eastern segment of the Azores-Gibraltar zone: The Gorringe Bank and the Gulf of Cadiz region, *Marine Geophysical Researches,* **19,** 211–230.

van Orman, J., Cochran, J.R., Weissel, J.K. & Jestin, F., 1995. Distribution of shortening between the Indian and Australian plates in the central Indian Ocean, *Earth planet. Sci. Lett.,* **133,** 35–46.

Wallace, M.H. & Melosh, H.J., 1994. Buckling of a pervasively faulted lithosphere, *Pure appl. Geophys.,* **142,** 239–261.

Wang, X. & Cochran, J.R., 1993. Gravity anomalies, isostasy, and mantle flow at the East Pacific Rise crest, *J. geophys. Res.,* **98,** 19 505–519 532.

Weissel, J.K., Anderson, R.N. & Geller, C.A., 1980. Deformation of the Indo-Australian plate, *Nature,* **287,** 284–291.

Wilson, D.S., 1989. Deformation of the so-called Gorda plate, *J. geophys. Res.,* **94,** 3065–3075.

Zukin, J.H. & Francheteau, J., 1990. A tectonic test of instantaneous kinematics of the Easter microplate, *Oceanologica Acta*, special vol. **10,** 183–198.